Link between respiratory pauses and vigilance states in freely moving mice

Authors: Giulio Casali[1]*, Camille Miermon[1]*, Geoffrey Terral[1], Pascal Ravassard[1], Tiphaine Dolique[1], Edith Lesburguères[1], David Jarriault[2], Frédéric Gambino[1], Nicolas Chenouard[1,3,#], Lisa Roux[1,#] (*shared authorship; [#]corresponding authors)

[1] Univ. of Bordeaux, CNRS, Interdisciplinary Institute for Neuroscience, IINS UMR 5297, 33000 Bordeaux, France

[2] Univ. Bordeaux, INRAE, Bordeaux INP, NutriNeurO, UMR 1286, F-33000 Bordeaux, France

[3] Sorbonne University, INSERM U1127, UMR CNRS 7225, Institut du Cerveau (ICM), 75013 Paris, France

Correspondence should be addressed to:
nicolas.chenouard@inserm.fr and lisa.roux@cnrs.fr

Abstract

Respiratory patterns share bidirectional links with brain functions: they are modulated by sensory stimuli, attention and emotions, are affected in some cognitive disorders, but they also can influence perception, emotions and cognition. In particular, brain activity undergoes drastic changes when switching between vigilance states, such as transitions between wake and sleep - as do the overall respiratory rate. However, how the fine features of respiration, beyond its rate, accompany these transitions remains unclear. To address this question, we equipped freely-moving mice with both intra-nasal pressure sensors and hippocampus-targeted electrodes. The unprecedented accuracy of the respiratory signals in mice spontaneously alternating between wake, non-rapid-eye-movement (NREM) and REM sleep revealed that periods of respiratory pause with low or no airflow, are interspersed within phases of exhalation and inhalation. If pause durations impacted the respiratory rate in individual states, the effect of pauses differed across sleep and wake. This stemmed from strikingly different patterns across states: mainly pauses after inhalation during wake, mainly after exhalation in REM, and a mixture of both for NREM sleep. We verified that respiratory patterns are distinctive signatures for states by building an accurate machine-learning algorithm relying solely on respiration information for the prediction of vigilance states. Our experiments demonstrated that the information of missing pauses after inhalation and of breathing variability were instrumental to precise REM sleep prediction. Moreover, results highlighted that these vigilance state-respiration relationships can be generalized across animals. In agreement, kinetic indicators for exhalation and inhalation co-varied across states and were spared by animal-to-animal variations, while the duration of pauses after inhalation stood as an isolated, state-discriminant feature. Finally, dynamical analysis revealed that distinct breathing features adapt with different kinetics at the transition time points between different states, possibly accompanying distinct cortical changes. Our work therefore clarifies how different features of respiration, and in particular pauses in nasal airflow, are associated to the specific physiology of individual vigilance states and suggest new links with brain functions.

Introduction

While respiration is crucial for survival by its peripheral action (1), it also shares strong functional links with the brain (2-5) . On the one hand, respiration shapes brain function (6-10), influencing perception, internal states and cognition (3, 4, 11-16). On the other hand, respiratory patterns are influenced by brain activity as they are modulated by sensory stimuli (17-19), attention (19-27), emotions (28-32), and can be affected in several cognitive disorders (18, 33-38).

In physiological conditions, brain activity dynamically evolves alongside behavioral and/or cognitive demands yet, it undergoes some of its most drastic changes at the time of switches from one vigilance state to another, such as transitions between wake and sleep. In mammals, transitions also occur within sleep as the brain alternates between Rapid-Eye-Movement (REM) and Non-Rapid-Eye-Movement (NREM) sleep. These two sub-stages of sleep can be identified based on electrophysiological (LFP or EEG) and muscular activity (EMG): NREM sleep is typically associated slow wave activity in the EEG while REM sleep is characterized a desynchronized EEG, rapid-eye-movements and overall low muscular tone (39-42).

Given the intricate brain-body relationships, changes between Wake, NREM and REM states are accompanied by significant modifications in the respiratory behavior, both in humans and animal species (7, 43-47). Overall, these past works have highlighted the fact that respiration rate and amplitude decrease during sleep as compared to wake, with REM showing higher respiration rates as compared to NREM (47). However, respiration is a complex behavior that can be described by many more features than rate and amplitude (48). For instance, the precise dynamics and volumes of inhalation *vs* exhalation are important features that also vary depending of vigilance states (44). Moreover, physiological pauses in respiratory activity – visible in human (48) and rodent (49) respiration recordings - are intriguing phenomena that could potentially relates to brain state transitions.

How do the fine features of respiration co-vary relative to one another in 'natural' conditions? How do they behave when an animal is undergoing transitions between wake, NREM and REM sleep? Are they a simple consequence of brain activity changes? Or do they precede the transitions undergone by neuronal networks?

Methodological advances based on pressure sensors that allow a precise monitoring of nasal airflow in rodents (50-53) and the development of new analysis pipelines dedicated to respiratory pressure signals (48) are offering an unprecedented opportunity to explore these questions. Using nasal pressure monitoring with electrophysiological recordings in the CA1 region of the hippocampus of freely moving mice, we found that respiration cycle features alone are strong predictors of brain states. Yet, machine learning-based prediction was less precise when pauses were left out. In line with this observation, we uncovered that respiratory pauses vary independently from other respiration features across breathing cycles and that they constitute an unexpected signature of brain states.

Results

Monitoring respiration and brain states in freely-behaving mice highlights changes of respiration kinetics across states

In order to measure mouse breathing with both high accuracy and minimal interference with the physiological alternation of vigilance states, we adapted a method for monitoring nasal air pressure (50) to feely-moving animals by using light and portable pressure sensors connected to intranasal cannula (**Fig. 1A**; **Methods**). Pressure sensors, unlike thermocouples (**Supplementary Fig 1B**), were sensitive enough to detect fine changes in nasal airflow including during sleep states (**Fig. 1B-C**). We verified that the intranasal cannula implantation preserved basic olfactory capacity (odor detection test**;** **Supplementary Fig 1A**) (Mann-Whitney rank sum test: $P > 0.999$; cannula-implanted mice $n = 5$, sham mice $n = 7$) and spontaneous exploratory behavior (**Supplementary Fig 1A**). Following this validation of the respiration recording method, we simultaneously implanted mice with intranasal cannula and silicon probes targeting the CA1 region of the

dorsal hippocampus (**Fig. 1A**) for electrophysiological recordings since changes of the local field potential (LFP) across brain states are well characterized in CA1 (54-56). We used CA1 LFP in combination with locomotion/accelerometer signals to define the three main brain states (**Methods**): Wake (high locomotion and high theta/delta power ratio), NREM sleep (immobility and low theta/delta power ratio), and REM sleep (immobility with prominent theta-band increase) (**Fig. 1C**). The freely-moving conditions allowed us to monitor brain states and respiration throughout long (> 2h) periods of time as mice (n = 11) spontaneously alternated between these three brain states (mean ± SEM; Wake, 7211 ± 391 seconds; REM, 425 ± 39 seconds; NREM, 5847± 363 seconds; n = 76 sessions).

To analyze the collected nasal pressure signals, we modified the BreathMetrics toolbox (48) so that individual respiration cycles were temporally identified and characterized in each experimental session with comparable accuracy across brain states (mouse-BreathMetrics, see **Methods** and **Supplementary Fig. 2**). When computing the smoothed instantaneous respiration rate (cycles/sec) through time (time bin = 200 ms, σ = 400 ms) we characterized significant inter-state difference (**Fig 1D, left**), as expected (43, 44, 57), respiration was more rapid during Wake (respiration rate = 4.8 ± 0.1 cycles/sec; mean ± SEM) than during REM and NREM, the slowest state (NREM = 2.4 ± 0.1 cycles/sec, REM = 3.1 ± 0.1 cycles/sec). Thanks to the precision of the pressure signal, we next focused on the dynamics of respiratory waveforms which comprised rapid alternations between negative and positive nasal pressures, inhalation and exhalation, respectively (**Fig. 1B**). Overall, the durations of inhalation and exhalation inversely scaled with the changes of respiration rates across vigilances states, as one might expect (**Fig. 1D**, right panels): inhalation (inh.) and exhalation (exh.) were the shortest during Wake (inh. mean duration = 60.9 ± 1.0 ms; exh. mean = 71.2 ± 1.2 ms), the highest rate state. Inhalation was also shorter during REM as compared to NREM (NREM inh. = 157.9 ± 3.2 ms, REM inh. = 139.8 ± 3.1 ms), but exhalation duration was not different (NREM = 131.2 ± 2.0 ms, REM = 136.8 ± 4.2 ms) as the variability of durations was increased during REM. The inhalation volumes were smaller when the respiration rate was faster (inh. volume Wake < REM < NREM) but in Wake, the reduction in volume induced by shorter

inhalations was in part mitigated by increased respiration amplitudes (Wake→NREM mean inh. duration +159%, inh. volume +59%) (**Supplementary Fig 3**). Changes of breathing rates across states also had limited impact on exhaled volumes (exh. volume (p.s.i. x ms) ± SEM: Wake = 75.8 ± 1.8 p.s.i. x ms, NREM = 70.6 ± 3.2 p.s.i. x ms, REM = 78.0 ± 4.7 p.s.i. x ms, $F_{(2,67)}$ = 3.2, P = 0.045) likely due to compensatory changes in respiration amplitudes (**Supplementary Fig. 3**). Overall, these data obtained with portable pressure sensors in freely moving mice confirmed the drastic changes in respiration rate between Wake and sleep and highlighted subtle differences between NREM and REM sleep.

Respiratory pauses are a prominent feature of respiration with a signature characteristics for brain states

If respiratory waveforms comprised inhalation and exhalation components, the high-quality intra-nasal pressure signals also showed flat periods after inhalation corresponding to no airflow (**Fig. 1B-C**, green shaded areas). Those respiratory 'pauses', similar to those observed in humans (48), are hardly detectable with intranasal thermocouples and difficult to delineate with whole-body plethysmography (**Supplementary Fig. 1B**). After exhalation, sudden slowdown in the airflow induced inflection points in the pressure signal in some cycles (**Fig. 1B**, orange shade). Those periods of low airflow were referred to as 'pauses after exhalation' and detected by mouse-Breathmetrics based on these inflection points (**Methods**). Pauses occurred at both ends of inhalation and exhalation, but not inside, and were observed in all vigilance states, even though exemplar respiratory traces suggested distinctive differences across states (**Fig. 1C**): pauses often appeared after inhalation in Wake, in contrast to REM, where they were mostly found after exhalation. NREM laid in-between, showing both types of pauses. We therefore undertook a systematic quantification of pauses after both inhalation and exhalation across brain states.

In agreement with our preliminary observations, population analysis demonstrated that during Wake, pauses predominantly followed inhalation (mean duration ± SEM = 72.0 ± 1.5 ms) and were practically absent after exhalation (duration = 7.4 ± 0.6 ms) (**Fig. 1E**).

By contrast, during REM the pause pattern was the exact opposite with absent pauses after inhalation (duration = 5.7 ± 1.0 ms) and significant pauses after exhalation (duration = 49.3 ± 2.7 ms). Pause patterns during NREM were in between those two extremes with pauses being still prominent after inhalation (NREM = 73.7 ± 7.2 ms) but also present after exhalation (duration = 61.3 ± 4.2 ms). As a consequence, when the mean durations of pauses after inhalation and exhalation of individual recording sessions were plotted against each other, REM and Wake formed distinct, compact clusters close to vertical and horizontal axes (**Fig. 1F**). On the other hand, NREM spanned the full range of possible combinations between short and long pauses after inhalation and exhalation.

We next examined the hypothesis that long respiratory pauses are associated to low respiration rates. The comparison of the mean cumulated duration of pauses within cycles with the respiration rate indeed revealed a strong negative correlation across recording sessions (Wake, Pearson's correlation coefficient, $r = -0.85$ $P < 10e-4$; NREM, $r = -0.85$, $P < 10e-4$; REM, $r = -0.36$; $P < 0.01$) and indeed highlighted that respiratory pauses lower the respiration rate in each individual state. Yet, the duration of pauses and the respiration rate, unexpectedly, did not simply scale inversely with each other across states as measurements from all states did not fall along a single diagonal line (**Fig. 1G)**. Sleep states indeed showed a continuum of values which could suggest scaling and NREM, which had the lowest respiration rate (**Fig. 1D, G**), was the only state with long pauses up to 300 ms due to the combination of pauses after both inhalation and exhalation (**Fig. 1E**). However, Wake stood out of the line. In particular, even though the respiration rate was 55% larger in Wake as compared to REM (**Fig. 1D, G**), the total pause duration still spanned the same 0-110 ms range. It suggests that, during sleep, episodes with longer pauses indeed correspond to slower breathing, but that other rules link respiration rate to pauses during Wake.

In order to further characterize the prominence of pauses in each state, we next computed the fraction of time occupied by pauses within the respiratory cycle (**Fig. 1H**). In agreement with differences in duration (**Fig. 1E**), pauses that follow inhalation occupied 25.4 ± 0.4 % of individual cycles in Wake, 14.2 ± 1.1 % in NREM, but only 1.5 ± 0.3 % of the cycle in REM. In contrast, pauses that follow exhalation occupied 11.5 ± 0.7 % of

individual cycles in REM, 13.3 ± 0.8 % in NREM, but only 1.7 ± 0.1 % of the cycle in Wake (**Fig. 1H**). While the precise moment when pauses occur varies, we noticed that overall, the fraction of cycle occupied by pauses was surprisingly similar between Wake and NREM. Indeed, during NREM, the occurrence of pauses shrunk the time spent in inhalation and exhalation to 72% of the respiratory cycle duration (mean inh. fraction ± SEM = 39.0 ± 0.5 %, mean exh. fraction = 33.5 ± 0.8 %, **Supplementary Fig. 3**) as both types of pauses occupied the remaining 28% (**Fig. 1H**). Despite a two-fold increase in breathing rate and shorter pauses during Wake as compared to NREM (**Fig. 1G**), we measured that pauses still occupied 27% of the cycle duration on average (with inh. fraction = 33.4 ± 0.2% and exh. fraction = 39.5 ± 0.3 %) (**Fig. 1H**). Faster breathing was therefore not achieved through a reduction of the fraction of the cycle dedicated to pauses. By contrast, a distinctive feature of REM was the lowered fraction of the cycle occupied by pauses. It was reduced to 13% (pause after inh. fraction = 1.5 ± 0.3 %; pause after exh. fraction = 11.5 ± 0.7 %), but this did not translate into faster breathing as compared to Wake as the durations of both inhalation and exhalation were simultaneously extended (inh. fraction = 43.7 ± 0.5%; exh. fraction = 43.3 ± 0.9%) (**Fig. 1D, Supplementary Fig. 3**).

Our results therefore provide evidence that patterns of respiratory pauses are signatures of the three major vigilance states in freely-moving mice. These signatures did not have a straightforward link to the observed changes of respiration rates across states and therefore provide a complementary characterization of the breathing-brain state relationships.

Nasal pressure dynamics predict brain state

If respiration and brain states are intertwined, we reasoned that a machine learning algorithm should be able to decipher those links to accurately predict brain states based on pressure sensor signals. Coincidentally, such algorithmic tool could prove useful to the community for brain state annotation without electrophysiological data. To test this hypothesis, we built an artificial neuronal network and trained it under supervision with data collected from 65 recording sessions from 9 different mice (**Methods**). The training

set was composed of 10 respiratory features extracted from mouse-BreathMetrics blinded for states (**Methods**). To serve as ground-truth for algorithm training, each respiratory cycle was automatically annotated with its corresponding state (Wake, NREM or REM) thanks to the CA1 LFP signals that had been simultaneously recorded (**Methods**) (58). After normalization (log scale to down tune large but infrequent variations, unit-standard deviation and zero-mean) (**Supplementary Table 1**), the distribution of individual features displayed cross-state differences that were larger depending on the state and feature considered (e.g. inhalation and exhalation durations discriminate sleep vs wake, inhalation pause duration discriminates REM vs other states) (**Supplementary Fig. 4A**). As all 10 features showed a form of state-discrimination, we included all of them as inputs of the prediction algorithm. On top of their normalized values, we added their standard deviation (SD) over a local time-window (**Methods**) as they also showed differences across brain states (**Supplementary Fig. 4B**), but were altogether uncorrelated from the feature amplitudes (**Supplementary Fig. 4C**). This indicated that local feature variability captured another facet of the respiration-brain states relationship which could be exploited for state prediction. The resulting algorithm provides a prediction of the brain state (and a confidence indicator, as measured by the predicted state probability) associated to each single breathing cycle based on the 20 descriptors from this cycle and from its neighboring cycles (100 preceding and 100 following cycles, **Supplementary Fig. 5**).

To test how efficiently our network could predict brain-states, but also how the respiration-brain states links can be generalized between animals, we trained it on all mice but one and used this left-out mouse for validation (**Fig. 2A**). As shown for an example session (**Fig. 2B**), the network learned to predict brain states for mouse #3, even though data from this animal was excluded from the training set, hence highlighting the inference of generalized, cross-animal, rules for prediction. Long periods of Wake and NREM sleep were correctly predicted with confidence close to 1 (1 corresponds to maximal confidence). Lower confidence was observed at the transition between brain states and during REM sleep periods which were much shorter, even though all 6 REM episodes were correctly predicted.

We repeated the training procedure for all the 9 mice as validation animal (7 training repetitions for each animal) and assessed the prediction quality based on the median confusion matrix (**Fig. 2C**). We found that 94% of annotated Wake cycles were correctly predicted as Wake cycles; 94% of annotated NREM cycles were correctly predicted as NREM and 87% of REM cycles were correctly predicted as REM. The largest confusion was observed between NREM and REM: 13% of annotated REM cycles were predicted as NREM. However, none was wrongly assigned to Wake and only 1% of NREM cycles were predicted as REM. Similar patterns of confusion occur when considering individual matrices associated to different validation animals (**Fig. 2D**), but with minor differences which could reflect residual animal-to-animal variations which could not be compensated for. Interestingly, the confidence of the predictor was the lowest when the predictions were incorrect (confidence = 0.81 ± 0.16 SD), while the confidence was high and showed little dispersion when annotated states matched the prediction (confidence = 0.96 ± 0.08 SD) (**Fig. 2E**). Prediction confidence therefore provides a useful indicator for any analysis downstream of state prediction (a feature not traditionally available for possibly faulty manual annotations and automated state prediction from LFP), encouraging caution and increased scrutiny when it is low.

We completed the analysis of prediction performance by computing standard indicators of classification performance: recall, precision and F1-score (**Methods**) (**Fig. 2F).** Indicators were all ≥ 0.9 (maximum is 1) for NREM and Wake states, proving an excellent ability to recover a large fraction of the correct states (recall) but also minimal contamination of the predicted states by others (precision). REM state was the most challenging, likely because this state's periods are shorter and less frequent in the training sets, but indicators were still all ≥ 0.8. Finally, we investigated how different respiration features impacted on prediction performance when they were left out of training and prediction (**Fig. 2G,** see also analysis of variance, ANOVA, statistics in **Supplementary Table 2**). We discarded them by groups of features as some were strongly co-varied (**Supplementary Fig. 4C**). Discarding kinetic measurements of inhalation and exhalation (durations and time to trough and peak) was compensated for by other features and did not result in degraded prediction. Volumes and flow information for inhalation and

exhalation only slightly lowered the recall of REM cycles (median value over animals = 0.83, down from 0.87 for no exclusion, ANOVA P = 0.005). A more striking effect was performance degradation for all indicators of REM prediction, in particular lower prediction precision (median value -9%, P < 0.001), when respiratory pauses were excluded from the inputs. The lack of compensation suggests that pauses are uncorrelated from other features, and that this unique feature of respiration is highly predictive of REM state. Overall, the strongest performance degradation was observed when local SDs (these reflect the amplitude of the variations for a given parameter among 10 neighboring cycles; see **Methods**) of all parameters were excluded from the inputs, with significant impact on both NREM and REM F1-scores (NREM median -2%, P < 10e-5; REM median -24%. P < 10e-18). Decreased NREM precision (0.68 median value, down from 0.81, P < 10e-5) stemmed from poor recall of REM cycles (0.68 down from 0.87, P < 0.0001) which could be wrongly predicted as NREM. These results therefore confirmed what the cross-state distributions of SDs suggested (**Supplementary Fig. 4B,C**): changes of local stability of respiratory features, beyond their amplitudes, are distinctive characteristics of sleep states.

Overall, these experiments highlight the existence of general, cross-animal, rules that link breathing features to brain states, and that those links are spread over multiple breathing features and their dynamics.

Distinct co-variant respiratory features encode brain states and animal identity

The stability of performance for state prediction obtained when excluding parameters (**Fig. 2G**) suggested that some features of breathing cycles co-vary as states alternate (i.e. some excluded parameters could be compensated by others), while other features behave more independently and may bring distinctive information about vigilance states. In particular, pauses uniquely discriminated REM sleep (**Fig. 2G, Supplementary Fig. 4A**). To clarify those covariations we computed the cycle-to-cycle Pearson's correlation matrix (**Fig. 3A**) of the 10 log-normalized features characterizing respiration (**Supplementary Table 1**) after balancing the proportion of brain states (1/3 of total

dataset each) (**Methods**). Feature correlations showed diagonal blocks with overlaps: volume related features (peak/trough flow and inhalation/exhalation volumes) formed one co-varying block. Kinetic measurements of inhalation and exhalation (durations, time-to-peak and -to-trough) formed another, but they showed a positive correlation with inhalation and exhalation volumes and the duration of pauses after exhalation. Interestingly, duration of pauses after inhalation stood isolated, mainly uncorrelated with other features of respiration. Covariance matrices obtained for individual states showed similar results (**Supplementary Fig. 4C**, right panels). Principal component analysis (PCA) of the data of the combined 3 states confirmed these observations: the first principal direction (PC1), explaining more than 42.6% of the total variance (**Fig. 3B**) was mainly supported by kinetic features of inhalation and exhalation and the duration of pauses after exhalation. PC2 was mainly supported by volume and flow features and explained 24.9% of the total variance, and PC3 (11.4% of total variance) mainly aligned to the duration of pauses after inhalation and, to a lesser extent, to time-to-peak during exhalation.

We next investigated two factors which could underlie the three first PCs by contributing to data diversity: brain state differences, but also animal-to-animal variations. Analysis of variance (ANOVA) of PC coefficients revealed that those two factors and their interaction all significantly contributed to data diversity for the three first PCs (P < 10e-6 for all factors). However, animal identity and brain states had different weights: for both PC1 and PC3 coefficients the F-statistics was much larger for the brain state factor (F_{state} = 18256, F_{animal} = 77, $F_{state\ x\ animal}$ = 58 for PC1; F_{state} = 6732, F_{animal} = 163, $F_{state\ x\ animal}$ = 50 for PC3) showing its dominance, while animal identity was the most prominent factor for PC2 coefficients (F_{state} = 49, F_{animal} = 1482, $F_{state\ x\ animal}$ = 118). In good agreement with the ANOVA, the individual distributions of coefficients for the 7 analyzed animals overlapped prominently for PC1 and PC3, but clear animal-to-animal differences were visible for PC2 (**Fig. 3C**). This was confirmed when computing the predictive power of individual PC coefficients with respect to animal identity: PC2 entropy (**Methods**) was more than 7.9% lower (lower is more predictive) than that of PC1 and PC3 (**Fig. 3D**). Unlike animal identity, brain states were clearly discriminated by PC1 and PC3, but not PC2, when

considering the distribution of individual coefficients (**Fig. 3E**) or the state-predictive power as measured by entropy (**Fig. 3F**). The most striking difference for PC1 coefficients was between Wake *vs* sleep states, unlike PC3 which mainly differentiated REM vs NREM+Wake (**Fig. 3E**), hence highlighting differences in brain state coding for those feature components. The entropies for other, less representative PCs (**Supplementary Fig. 6A**) were not as marked as for PC1, PC2 and PC3 (**Fig. 3D,F**).

Overall the analyses of single cycle covariates revealed that: 1) kinetic features contributed the most to the variability of the data (PC1), were robust across animals and discriminated sleep and Wake states, 2) flow and volume features (best represented by PC2) varied across animals but less across states and 3) changes in pauses after inhalation (best represented by PC3) were an important feature of REM sleep.

Respiration rapidly adapts at wake↔sleep transitions but slowly at NREM→REM switches

We next asked how tightly breathing is linked to brain states by characterizing breathing adaptation in narrow time windows around state transitions. Using PC1 and PC3 to summarize breathing features linked to brain states (**Fig. 3**), we plotted time-series of coefficient values against that of brain states for an exemplar session (**Fig. 4A**). In agreement with the population analysis (**Fig. 3),** PC1 and 3 coefficients reached different plateaus (defined by specific values) when the cortical state changed and PC3 seemed more sensitive to entering/exiting REM than NREM sleep (i.e. PC3 showed larger differences between the plateaus surrounding the transitions to/from REM). Zooming in on three Wake→NREM transitions (#1,2,3) (**Fig. 4B**), PC1 coefficients sharply adapted (purple arrows) while PC3 coefficients were more stable. This was confirmed by pooling together coefficients from all Wake→NREM events (n = 1638, **Fig. 4D**): on average, the strong PC1 rise (mean value *post–pre transition* Δ_{PC1} = 3.67 a.u.) started within 50 cycles before the annotated cortical transition and plateaued within ~10 cycles after transition to NREM. PC3 values were more stable during Wake→NREM (Δ_{PC3} = 1.41 a.u.) (**Fig. 4E**). This observation matched with the lack of difference between these two states at the population level for the duration of pauses after inhalation (**Fig. 1E**; as these contribute

vastly to PC3, **Fig. 3A**). NREM→Wake transitions (n = 1276) mirrored that of Wake→NREM in coefficient amplitudes (Δ_{PC1} = -2.58 and Δ_{PC3} = -1.20) but PC1 adaptation shortly followed, rather than preceded, the state transition (**Fig. 4D,E**). Dynamics of individual respiratory features at state transitions matched that of their associated PC (but not as saliently) (**Supplementary Fig. 7**). Thus, these observations indicate that the fast changes in respiration cycle dynamics (largely represented by PC1 coefficients) precedes transitions to annotated NREM but that they lag behind at transitions to Wake from a NREM episode. In good agreement with the poor state discrimination for PC2 and the minor PCs 4 to 10 (**Fig. 3E,F**), coefficient changes for those were not only smaller than for PC1 (Wake→NREM Δ_{PC2} = 0.33; NREM→Wake Δ_{PC2} = -0.31) but they were also loosely time-aligned to the transitions (**Supplementary Fig. 6B**).

Exemplar NREM→REM transitions (#4,5,6) **(Fig. 4C**) showed strikingly different profiles for both PC1 and PC3 as coefficients adapted slowly (>100 cycles between observed plateaus). Interestingly, PC3 adapted early before the annotated cortical transition. On the contrary, the onset of PC1 adaptation was time-locked to the state transition (yellow arrows) and showed a progressive change over the course of REM cycles unless the REM episode was interrupted (see events #5 and 6). In fact, population averages showed that PC1 coefficient decay started at the onset of the transition but only lasted up to ~200 breathing cycles after REM started (corresponding to ~66 sec when considering that the average cycle duration is ~332 ms in REM) (**Fig. 1D**). This revealed that respiration cycle dynamics (inhalation and exhalation) are not steady when it comes to REM but that they undergo a progressive compression during the very first minute of a REM episode. PC3 coefficients (that mainly represent pauses after inhalation) also showed significant (Δ_{PC3} = -0.43) but slow adaptation. Unlike PC1 coefficients which decayed following REM onset, the mean trace for PC3 started to decay around 100 cycles *before* the NREM→REM transition (**Fig. 4E**). Interestingly, PC3 adaptation was interrupted by the state transition as no further decay was seen beyond 50 cycles in REM. By contrast with entry to REM sleep, exit from it to either NREM (n = 247) or Wake (n = 326) were rapid and mainly unanticipated for PC3 coefficients (**Fig. 4E**). For PC1,

changes were also unanticipated, but not as sharp (**Fig. 4D**). Overall, our data indicate that a progressive reduction in the duration of pauses after inhalation (reflected by PC3) consistently precedes REM entries. This is then followed by a slow decay in the inhalation and exhalation dynamics (reflected by PC1) for a relatively fixed number of cycles (~200) within REM.

Do the gradual and time-shifted adaptations of respiration features at NREM→REM precede the changes in hippocampal network activity? Could they be temporarily disconnected? To address this question, we directly compared the dynamics of hippocampal LFP *vs* breathing features (**Supplementary Fig. 8**). We first focused on the Wake→NREM and NREM→REM transitions, as these showed interesting respiration changes (**Fig. 4**). At Wake→NREM transitions, changes in normalized theta and slow-wave powers mirrored PC1 dynamics indicating that breathing kinetic parameters go hand-in-hand with neuronal activity: both progressively change before the animal falls asleep. At NREM→REM transitions, slow waves dynamics was again similar to PC1's (amplitude decrease time-locked to the transition but prolonged, up to 200 cycles, after REM onset). In contrast, we found that theta power starts to increase *before* (~100 cycles) the annotated transition and quickly stabilizes (<40 cycles) once REM had started. This dynamic resembles PC3 variations (and the reduction in pauses after inhalation; **Supplementary Fig. 7**) dynamics. This suggests that different breathing features coordinate with distinct cortical changes (i.e. PC1 with slow wave power, PC3 with theta power) that also occur gradually when animals enter REM sleep.

In summary, sharp respiratory adaptation when animals fell asleep highlighted a tight link between brain state and respiration. The picture was different at NREM→REM transitions where adaptation was more progressive and either anticipated or followed the annotated cortical change depending on the respiratory features (PC1 or 3). This suggests a more complex link between respiration and the mechanisms guiding the transition to REM sleep.

Discussion

In this study, we monitored hippocampal activity, head-acceleration and nasal pressure in freely moving mice equipped with portable pressure sensors. The precision of the pressure signal obtained revealed that respiratory cycles are not only composed of inhalation and exhalation components, but also of respiratory pauses corresponding to low or no airflow. Our analysis indicated that the duration of these pauses is variable and represents an independent feature of respiratory cycles. The position of pauses with regards to inhalation and exhalation was specific for each brain state: in wake, they mostly occur after inhalation, while they follow exhalation in REM sleep and were found in both locations during NREM. When predicting brain state based on respiration features, we found that respiratory pauses contribute the most to the prediction precision for REM when compared to other features. In line with this observation, we found that transitions between vigilance states are accompanied - and sometimes preceded - by changes in respiratory pause duration, pointing towards a shared mechanism. Overall, this work shows that pauses in nasal airflow are key components of the respiration cycles that contribute to the specific physiology of individual vigilance states.

Monitoring respiration in naturalistic conditions

Because of the central role of respiration for sensation and cognition, several methods have been developed over the years to monitor respiration in parallel with brain function in animal models (59-65). In head-fixed rodents pressure sensors connected to nasal cannula have allowed studying respiration-driven neuronal activity with high precision (50-53). Yet, measuring nasal pressure has remained challenging in freely moving mice, especially when it was combined with neuronal recordings (but see (19, 44). In these conditions, a commonly used method consists in measuring variations of nasal temperature using thermocouples or thermistors (26, 62, 66-69). Alternatively, respiration can be monitored *via* whole-body plethysmography (31, 70, 71). Yet, these methods are not ideal when studying animals in freely moving conditions: thermocouples provide massively attenuated signals during sleep (in our conditions, the signal non-exploitable in this state, **Supplementary Fig. 1B**) and plethysmography restricts rodents

to small hermetic enclosures and are thus incompatible with naturalistic behaviors. Most importantly, both of these approaches do not allow a precise detection of respiratory pauses that can only be revealed with accuracy through the use of pressure sensors. As respiration is a strong modulator of brain activity (2, 3, 8, 28, 72) and has been proposed to act as a widespread synchronizer of neuronal networks (7-9), the methodology proposed here based on portable pressure sensors therefore represents a valuable tool for re-evaluating those results with improved respiration monitoring and in light of the prominence of respiratory pauses.

Scoring vigilance states with nasal pressure signals

Because the assessment of vigilance states is central to basic and clinical studies, a large numbers of automatic scoring methods have been developed, both for human and rodent models (reviewed in (54)). Most approaches rely on a combination of neuronal and movement signals (e.g. coming from electroencelography – EEG - electrodes and electromyograms - EMG) but one study proposed to use only local field signals from the hippocampus and the olfactory bulb (6). Given the strong link between respiration and neuronal activity in the olfactory bulb (4, 20, 73-75) and the hippocampus (7, 68, 76, 77), the success of the latter approach is likely linked to the known changes in respiratory patterns across brain states (43, 44, 57). Another study showed that qualitative visual scoring of vigilance states based on whole-body plethysmography was in good agreement with manual scoring based on EEG and EMG data of individual mice (78). Yet, whether respiration changes are consistent across animals and whether these could be used, without additional information (such as EMG), to predict vigilance states was still unclear. Here we present a machine-learning-based method that provides automatic and accurate prediction of vigilance states solely based on nasal pressure signals (**Fig 2**). Our results parallel those from a recent computer vision method for vigilance scoring which relied partly on visual features in videos which could reflect breathing (79). Video-based assessment of respiration was however limited to the rate and our precise characterization of the components of respiratory waveforms, including pauses, can explain the superior performance of our approach for REM detection (**Fig. 2**). Moreover, we show that unlike amplitude features, the temporal properties of the respiration

components are comparable across animals (**Fig 3**). This consistency likely allows our algorithm to provide an accurate prediction of vigilance states in new animals that were not part of the training set. The pre-trained network, thanks to its accuracy and generalization capability, could be applied to other datasets and become a valuable asset for state scoring based on respiratory pressure signals solely, without requirement for electrophysiological recordings.

Mechanisms of respiratory pauses

A wealth of studies addressing the neural basis of breathing allowed to establish a solid theoretical framework pointing at brainstem subnetworks as critical for respiratory rhythm (1, 80-82). In particular, the pre-Bötzinger complex (pre-BötC) is considered crucial for driving inhalation whilst the retrotrapezoid nucleus/parafacial respiratory group is known to orchestrate active exhalation. Recent evidence showed that immediately after the inhalation - an epoch termed “post-inspiratory phase of breathing” - a dedicated subnetwork of excitatory neurons with autonomous rhythmic properties termed post-inspiratory complex is recruited (83). Based on this discovery, the “triple oscillator” hypothesis has been proposed where the three phases of breathing are governed by distinct brainstem subnetworks (82). In this framework, our report of Wake respiratory pauses occurring after inhalation seem consistent with the concept of the post-inspiratory phase, and it is plausible that PiCo neurons are involved in driving pauses during Wake. Yet, the fact that pauses show variable durations partially challenges the view that respiration results from a pure oscillatory phenomenon. Based on our results, we propose instead that mice can block outgoing exhalation airflow after inhaling, and that this blockade dominates during wakefulness in freely-moving conditions. The neural mechanisms at play during these pauses have to be further studied in light of sensitive pressure sensor recordings.

During sleep, we could characterize a slowdown in outgoing airflow (which defines pauses after exhalation), unlike during Wake when exhalation is instantaneously followed by the next inhalation. The fact that REM sleep is characterized by muscular atonia and that REM sleep only shows this type of pauses, points towards a passive mechanism. We suspect that the inflection detected in the pressure signal (that defines pause onset)

are related to the physical properties of the lungs that passively deflate following inhalation. Our results indicate, unexpectedly, that such deflation hardly happen in awake freely moving conditions (pauses after exhalation, on average, only represent 1.7 % of the cycle).

Respiration in sleep

Consistent with other studies (7, 43, 44, 57), we found that the respiratory rate during sleep was decreased compared to Wake (**Fig. 1D**). Similarly, we observed that pressure dynamics differed between Wake and sleep, with Wake cycles being on average shorter in duration and with more prominent inhalation/exhalation peaks (**Fig. 1D**, **Supplementary Fig. 3**). Interestingly, we also found several differences between NREM and REM sub-states (**Fig. 1,3**, **Supplementary Fig. 3**), notably with regards to pauses. Those differences were discriminant enough to accurately predict brain states (**Fig. 2**), but with degraded precision for REM when pauses were omitted (**Fig. 2G**). State prediction experiment also uncovered that the local stability of respiration parameters (as measured by their local SD) strongly discriminates states, and in particular REM (**Fig. 2G**). Local stability, however, showed only weak correlation with the amplitudes of the respiration parameters (**Supplementary Fig. 4C**) and may therefore reflect a parallel set of mechanisms linking respiration to vigilance states.

We went further by revealing the dynamic or respiration features at the transitions between states. We found that pauses after exhalation become progressively shorter ~100 cycles before the animal enters REM sleep (**Supplementary Fig. 7I, Supplementary Fig. 8B**), mirroring the progressive increase in hippocampal theta power. We hypothesize that the hypothalamic networks involved in the regulation of REM sleep onset (39, 42) are linked to the neuronal circuits regulating respiration pauses. Future work is required to unveil the modalities of this potential interactions at the transitions between sleep sub-stages.

Interestingly, NREM sleep is the state when central sleep apneas are most commonly observed in humans (84) and mice (85). Although they occur at very low rate (~22 apneas/hr in mice with the most permissive detection criteria (86)) as compared to the pauses we study here (present in nearly all breathing cycles), apnea events have been

shown to occur at the end of exhalation, similar to the pauses we identified during sleep. It raises the possibility that central sleep apneas, which affect sleep quality and are linked with cardiovascular dysfunctions (87-89), share similar mechanisms with the physiological respiratory pauses highlighted in our study. Working on the neuronal substrates involved in sleep and respiration regulation could therefore improve our understanding of the mechanisms underlying detrimental breathing disorders in sleep.

Methods

Animals

All experimental procedures were performed in accordance with standard ethical guidelines (European Communities Directive 86/60-EEC) and approved by the local committee on animal health and care of Bordeaux and the French ministry of agriculture and forestry (authorization numbers 18625, 19746, 23974 / facility agreements A33063940 and A33 063 943). All mice were maintained in pathogen free facilities in a diurnal 12h light/dark cycle with food and water ad libitum. A total of 11 mice were used in this study: 9 C57bl6/J male, and 2 OXT-IRES-cre female mice.

Pressure sensor

Pressure sensors (PS) were purchased from Honeywell (part #: SSC S RN N 004ND AA5). Our protocol is based on a previous approach (50) that we adapted to recordings in freely moving mice in two ways. First we added a 6 pin male connector below the PS to fit a 6 pin female connector cemented on the head of the animal. This ensured a stable fixation of the PS during recordings in freely moving mice. Second, we soldered the input and output electric connections of the PS to thin Litz wires which were themselves held by a pulley system ensuring very low weight on the head of the animal. A piece of polyethylene tubing (801000, A-M Sys-tems, ID 0.015in, OD 0.043 in) of adjustable length allowed to connect the PS port to the nasal cannula. During inhalations, the inward flow of air into the nose causes a decrease in the measured pressure. During exhalations, the outward flow of air from the nose results in an increase in the measured pressure. Besides these inhalation- or exhalations-induced deflections, flat pressure signal corresponds to atmospheric pressure and respiratory pauses.

Nasal cannula

Nasal cannulas were home made from 23G hypodermic stainless steel tube (A-M Systems). Briefly, the tube was cut to an 8mm length and the tip was beveled with a 45

degrees' angle. A mark at 1.5 mm from the beveled tip symbolizes the limit for insertion during surgery. To ensure that cannulas do not get blocked by dust or litter between recording sessions, they are capped with dummy plugs when animals are not being recorded. Dummies consist in 11mm long 27Gx1/2'' industrial dispensing tip (CML supply). Only 2mm of plastic is kept from the top of the dispensing tip to allow for an easy removal by the experimenter. On this dummy a 3mm piece of 23G stainless steel tube and an 8mm of polyethylene tubing (801000, A-M Systems, ID 0.015in, OD 0.043 in) are glued to the base. The 3mm tube acts as a stopper to ensure that the dummy does not exceed the length of the cannula, and the polyethylene tubing holds the dummy onto the cannula.

Thermocouples

Thermocouple-based measurements of respiratory behaviors rely on the fact that the body temperature of mice (38℃) is warmer than external temperature in our recording conditions (20-24℃). During inhalations, the inward flow of external air into the nose causes a decrease in the measured temperature. During exhalations, the outward flow of air from the nose results in an increase in the measured temperature. Here we used K-type thermocouples (Omega) inserted in the nasal cavity of mice and cemented in place on the skull (see below).

Surgery

Surgeries for local cannula implantation were performed as previously (Smear et al 2011). For local cannula implantation, mice were anesthetized using isoflurane (induction 3 minutes at 4%, then at 1.5% during the surgery). They received an intraperitoneal injection of an analgesic (Metacam, 5mg/kg) and hair above the skull was removed using a hair removing cream (Veet). Mice were then placed on a stereotaxic frame (RWD) where vitals (body temperature, heart rate, blood oxygenation level) were tracked using PhysioSuite (Kent Scientific). The eyes were protected against dryness with Vaseline. A midline incision was performed above the skull and the nasal bone following a local subcutaneous injection of 0.1ml of lurocaine (5mg/kg). The skull was cleaned of

any conjunctive tissue using a micro-curette (Fine Scientific Tools). A dental drill (small size) was used to perform a craniotomy in the nasal bone. We advise to perform the craniotomy with a single and franc movement of the drill ensuring effective opening of the nasal epithelium membrane located right below the nasal bone. During this delicate step, it is important not to touch the turbinates located below the hole with the drill tip to prevent any subsequent clogging of the cannula. Coordinates for optimal respiratory recordings (AP = 3.5-4, ML = 0.5, DV = 1.5mm) were defined from the junction between the midline and the fronto-nasal sutures (but these can potentially vary depending on the mouse strain and age). During insertion, the beveled tip of the cannula was oriented towards the midline to increase successful signal collection. We also advise to implant the cannula with its dummy to avoid any blood or tissue to enter the cannula during insertion. Nasal cannula is then fixed to the bone via Superbond (C&B), and a 6 pin connector is cemented on the back of the skull to allow attachment of the pressure sensor in subsequent recordings (see Pressure sensor section). Finally, a handle is cemented on the skull to facilitate the immobilization of the mouse during pressure sensor attachment and the skin is closed with Vetbond (3M). Sham animals used in the odor detection task (**Supplementary Fig. 1**) underwent the same surgical procedure except that no craniotomy was performed and the cannula was cemented at the surface of the skull, above the nasal bone.

For 7 mice, high density silicon probes (Buzsaki 32, NeuroNexus) were implanted in the CA1 region of the hippocampus (AP = -1.8, ML=1.4, DV = -1.2). The local field potentials recorded in this region combined with the accelerometer signal obtained from the Intan headstages (RHD 32ch, Intan), allowed brain-state annotations.

For the comparison of the signals obtained from PS and thermocouple (K-type TC, Omega), two symmetrical craniotomies were performed above the nasal bone at the same AP coordinates as for PS implants. PS was implanted as described above. For TC, removal of the nasal bone was performed by progressively thinning the skull with gentle drilling until the highly irrigated nasal epithelium membrane was revealed. The membrane was pierced with a fine cotton tip, creating the hole required to insert the TC 1.5mm deep into the cavity. The craniotomy was then protected with Kwik-Sil (WPI), and the implant

was stabilized with Superbond (C&B). For brain state detection, electroencephalogram (EEG) signals were collected using a miniature screw implanted in the cortical bone and referenced to a ground screw above the cerebellum.

Plethysmograph

Whole-body plethysmography (31, 70, 71) provides a non-invasive biomechanical measure of respiration. Here, a whole-body plethysmograph chamber (Emka Technologies, France) was used to record mouse respiratory activity in parallel with nasal pressure monitoring. Mouse breathing induces pressure changes in the plethysmograph chamber. These were captured by a differential pressure sensor that compares pressure in the animal chamber with the reference chamber. Constant airflow (2.2 L/min) was provided through the apparatus. The respiratory signal collected from the plethysmograph was interfaced to a computer equipped an Intan acquisition board (see Data acquisition section).

Data acquisition

Pressure sensor, thermocouple and plethysmograph signals were acquired continuously at 20 kHz on an Intan RHD2000 interface board analog input channels (Intan Technologies). A voltage divider was placed between the pressure sensor and the acquisition board to insure that the voltage range was not exceeding 3.3V. Thermocouple signal was amplified before acquisition (amplification factor: 192). Electrophysiological signals were simultaneously acquired at 20 kHz after being amplified by 32 and 64-channel digital headstages (Intan Technologies).

Brain state scoring

Since past studies have demonstrated that the presence of hippocampal theta oscillation in an animal with sleeping posture is sufficient to identify REM sleep (90), epochs of Wake, Rapid eye movement sleep (REM) and non-REM (NREM) have previously been defined using the ratio of the hippocampal LFP power in theta band (5–11 Hz) and delta band (1–4 Hz) combined with motion signal (55, 91). Similarly in our

study, Wake, REM and NREM episodes were annotated offline using the ratio of the hippocampal LFP power in theta band (5–11 Hz) and delta band (1–4 Hz), the accelerometer signal as well as visual inspection of raw traces and whitened power spectra (using a low-order autoregressive model), but with the help of a Matlab GUI (*TheStateEditor* from the Buzsáki Lab repository - https://github.com/buzsakilab/buzcode/blob/dev/GUITools/TheStateEditor/TheStateEditor.m) (56). Several previous studies have demonstrated that the presence of hippocampal theta oscillation in an animal with sleeping posture is sufficient to identify REM sleep (90).To label breathing cycles used to train the artificial network, we used an automatic state scoring approach described previously that similarly relies on spectral features and motion signal (58) (StateScoreMaster from the Buzsáki Lab - https://github.com/buzsakilab/buzcode/blob/dev/detectors/detectStates/SleepScoreMaster/SleepScoreMaster.m).

Pressure sensor data analysis

All analyses were performed using MATLAB (The MathWorks) built-in functions, the FMAToolbox (http://fmatoolbox.sourceforge.net/), Buzsaki lab toolbox – *buzcode* (https://github.com/buzsakilab/buzcode), the freely available MATLAB toolbox from the Zelano lab *BreathMetrics* (https://github.com/zelanolab/breathmetrics) and custom-written scripts.

Respiration was analyzed *post-hoc* using a modified version of BreathMetrics, a toolbox designed to automatically describe respiratory features from pressure sensor signals acquired from human or rodent subjects (48). We called this modified version “mouse-BreathMetrics” to acknowledge the contribution of the original script and highlight the fact that our script was only tested on mouse data. Here, we used *BreathMetrics* with a redundant re-iterative approach aimed at maximizing the number of respiratory cycles. This was done in order to both account for signal instability of our recordings (baseline drift, electrical noise, transient loss of signal) and to prevent potential artefacts due to radical changes in the respiration pattern across behavioral states. Briefly, the steps

followed to analyze respiratory signal of each session are summarized here and can be visualized in **Supplementary Fig. 2**.

Firstly, the respiratory signal was examined by the experimenter to ensure that only intervals with valid data, “valid sniff-blocks”, were taken into account (ex 0-20s, 40-80s, 95-160 etc in **Supplementary Fig. 2** Ai). This step was only necessary for sessions with transient nasal cannula clogging that results in pressure signal loss.

Secondly, valid sniff-blocks were intercepted with brain states (see **Supplementary Fig. 2** Aii Wake: 0-60 seconds, 200-240 seconds, 280-300 seconds; NREM: 60-140 seconds, 160-200 seconds, 140-260 seconds, 240-255 seconds, 260-280 seconds; REM: 140-160 seconds, 255-260 seconds) previously detected using hippocampal LFP spectral features (theta/delta ratio) and accelerometer (movement) as previously described (see **Brain state scoring** section of **Methods**)(56). The resulting “sniff-chunks” contained homogeneous signal belonging to only one behavioral brain state (see **Supplementary Fig. 2** Aiii; Wake chunk: 0-20 seconds, 40-60 seconds etc; NREM chunk: 60-80 seconds, 95- 140 seconds; REM chunk: 140-160 seconds, 255-260 seconds).

Thirdly, each sniff-chunk was individually analyzed using *BreathMetrics* (**Supplementary Fig. 2** Bi), so that a preliminary characterization of the respiratory cycles could be obtained (**Supplementary Fig. 2** Bii). However, we noticed that errors in the detection of the onset/offset of the respiratory components were frequently encountered mostly due to the inaccurate pause detection. More rarely, respiratory cycles were found to be “skipped” due to short epochs of baseline-drift in the raw signal, heavily altering the quality of the results during those short windows. To account for this, we used BreathMetrics with a redundant re-iterative approach to maximize the number of respiratory cycles in each sniff-chunk. We further split each sniff-chunk in “sniff-lets”, short time intervals containing the signal of 10+1 pre-detected respiration cycles (see **Supplementary Fig. 2** Ci). Theoretically each sniff-let contained 11 cycles but this was ensured by iteratively altering its signal with a moving-average window correction of increasing size (20 iterations, window size 1-3 seconds). In each iteration, the altered signal was run with *findExtrema* from *BreathMetrics* toolbox yielding each time the

number of detected respiratory cycles. At the end of 20 iterations, the altered signal with highest number of sniff cycles was chosen for the next steps – otherwise the raw signal was maintained. Once ensured each sniff-let contained the highest number of cycles, the signal was re-examined using the following functions from *BreathMetrics* toolbox:

Breathmetrics
correctRespirationToBaseline
findExtrema
findOnsetsAndPauses
findInhaleAndExhaleOffsets
findBreathAndPauseDurations
findInhaleAndExhaleVolumes

In order to obtain a finer detection of respiratory components (in particular pauses during wake state), we took into account minima and maxima of the sniff-let raw signal first derivative reflecting troughs and peaks in the rate of instantaneous pressure (see **Supplementary Fig. 2** Cii).

In each sniff-let, inhalation and exhalation were re-calculated after pause detection which were assigned if the following criteria were simultaneously met (see **Supplementary Fig. 2** Ciii):

a) pressure signal in the 5-95th percentile range during previously assigned pauses epochs of the entire sniff-chunk;
b) first derivative in the mean + standard deviation of the first derivative signal during previously assigned pauses epochs of the entire sniff-chunk;
c) outside of the window between ascending peak and descending through of the first derivative of the sniff-let (putative inhalation);
d) outside of the window between descending through and ascending peak of the first derivative of the sniff-let.

Single-cycle data normalization and analysis

We analyzed single-respiratory-cycle properties of recordings from 8 animals (males and females): id 3C030 (16 sessions), 3C060 (8 sessions), 3C209 (4 sessions), 3C210 (2 sessions), 7C012 (13 sessions), 7C014 (8 sessions), 7C026 (10 sessions), 7C026 (2 sessions), 7C029 (3 sessions). Brain states were annotated using the method described above with CA1 LFP signals that were simultaneously recorded.

For the machine learning-based approach (**Fig. 2-4**), in order to make the algorithm solely based on respiration signal, we ran BreathMetrics on each valid sniff-block, without breaking out the signal into state-specific chunks, hence making cycle detection and feature extraction state-blind. The same analysis pipeline as the one described above was conducted. Respiratory features extracted by *BreathMetrics* were: 'peakInspiratoryFlows', 'troughExpiratoryFlows', 'inhaleTimeToPeak', 'timeToTroughs', 'inhaleVolumes', 'exhaleVolumes', 'inhaleDurations', 'exhaleDurations', 'inhalePauseDurations', 'exhalePauseDurations'. To allow for principal component analysis (PCA) and state prediction each feature values were first log-normalized to make their distribution Gaussian-like (x'=*log (x + 10e-4)*). Then, each log-feature was centered with respect to the median of each animal mean value (m) (n = 9) (computed over all its cycles) and normalized by the median of each animal standard deviation value (s). Normalization parameters (**Supplementary Table 1**) were fixed *a priori,* and were used unchanged for all sessions from all animals. Doing so, the standard deviation of each feature was approximately (but not strictly) 1 for each session and each mean was approximately 0.

For automated brain state prediction (**Fig. 2**) log-features were augmented by their temporal standard deviation (SD) over a local time-window of size 10 cycles. Those SDs were themselves centered and unit-variance normalized (**Supplementary Table 1**). In this case we used automated state annotation as provided by the method described above so as to avoid expert-to-expert differences and inconsistencies which cannot be learnt.

Principal component analysis of single cycle variations (**Fig. 3** and **Supplementary Fig. 6**) was performed by singular value decomposition of the covariance matrix of the normalized features. The latter matrix was obtained by equally sampling cycles in

sessions from all animals (1000 cycles for each animal-brain state pair) except for 7C026 which showed very little sleep and almost no REM cycles. Entropy values in **Fig. 3D** were computed by building a histogram of PC coefficient values with 200 equally spaced bins and then computing for each bin the empirical probability p_j = *Pr(animal id|coefficient value in bin #j)* based on the proportion of animals associated to the coefficient in the bin #j. The entropy of this bin was computed as $-p_j log(p_j)$ and the total entropy was the weighted sum of the entropy values of all bins, with the proportion of coefficients falling in a bin as its weight. The same procedure was applied for entropy values in **Fig. 3F**, but the empirical probability p_j = *Pr(brain state|coefficient value in bin #j)* was computed and used instead.

Automated brain state prediction with artificial neural networks

We designed an artificial network specialized for brain state prediction as shown in **Supplementary Fig. 5.** It takes 201 breathing cycles described by the 20 normalized features as inputs and the output layer combines both local (first convolutive layers) and contextual information (last convolutive layers) to compute the probabilities of each three states.

As a final step, state probabilities are smoothed using a temporal Gaussian filter (with σ = 20 cycles) and the predicted state is taken as the one with maximal probability. The confidence in the prediction is computed as this predicted state probability so that confidence is high when the differences between state probabilities are large.

The algorithm was implemented using a Jupyter notebook with Python. Numpy and Scipy libraries are mainly used for mathematical computation. The proposed artificial neuronal network structures are implemented thanks to the TensorFlow (2.0.0) dedicated library with GPU support. 2733 free parameters need to be adjusted for best prediction performance.

Network parameter optimization was carried out using sessions from 8 animals, leaving one out for assessing data overfitting and for validating the ability of the network to infer generalized properties of breathing features and brain states to other animals. Training was repeated 9 times, cycling through different animals for validation. Parameter

optimization was performed by minimizing the categorical cross-entropy between the discrete annotations of states (ground-truth) and the continuous prediction of their probabilities by the network. To cope for the imbalance between the frequency of each state (REM being the rarest), different weights were used for the prediction of sates: 0.1 for wake cycles, 0.25 for NREM, and 0.5 for REM. A gradient-descent-type algorithm (Nadam) was used with learning rate 10e-5. We re-sampled 20 times (outer epochs) 2000 random cycles from each animal (all sessions) to limit memory usage. 3 steps of gradient-descent were performed with those 2000x8 = 16000 cycles (inner iterations). For training only, 'dropout' (with a rate of 10%) layers were inserted between the layers to regularize the optimization problem and thus limit data overfitting. 7 independent networks were trained for results averaging in **Fig. 2C-F**. 5 networks were trained for each condition in which some input features were excluded from training and validation (**Fig. 2G**).

Explorative odor detection task

The explorative odor detection task was adapted from previous studies (92). Briefly, the materials used consisted of a test cage similar to the home cage but with an odor holder that was made from a stainless-steel lid of an unused mouse water bottle. The bottle lid fit flush in a hole which prevented it from being displaced by the mice during the test. The tip of the lid's nozzle extended 5cm and contained a 3mm hole from which odors could emanate. Cameras were installed above the test cage and on each side of the odor holder to allow easier visualization**.** The cage was placed on a table in a dedicated testing room (separate to the housing room).

The behavioral protocol consisted of 2 days of habituation to the test cage before the test day. Each mouse was placed in the test cage for 3 minutes each of 5 separate trials for the odor detection experiment with a 3-minutes inter-trial interval. Before each trial, 10 µL of mineral oil was placed on a 2cm strip of filter paper and placed in the odor holder. All mice were water deprived after the 2nd day of habituation for 24 hours before the test to increase their motivation to explore.

Based on a serial dilution method with mineral oil, increasing concentrations of the odor (Isoamyl acetate [banana-like (Sigma-Aldrich)]) was tested as follow: mineral oil,

0.001%, 0.01%, 0.1% and 1%. 10µL of these solutions were placed on a strip of filter paper immediately before each trial and then introduced inside the nozzle of the odor holders. The odor holders were cleaned with 4% sodium bicarbonate and water between trials and experiments.

The time mice spent investigating the presented odor was counted manually using a customized program (BehavScor v3.0 beta): considered epochs corresponded to the time intervals when mice directed their nose <1cm from the tip of the holder. Mice exploring less than a total of 5 seconds within the 5 trials were excluded from the analysis and each animal was tested only once with a single odor. The odor threshold was defined as the odor concentration the most explored or the lower odor concentration for which the mice spent less than 10% to investigate it as compared to the most explored concentration.

Statistical Analyses

Statistical analyses were performed using MATLAB scripts. Most comparisons were performed using repeated measure ANOVA tests. For *post-hoc* tests, Bonferroni corrections were applied to account for multiple comparisons. Additional nonparametric tests (Mann-Whitney U tests, Kolmogorov-Smirnov tests or Wilcoxon signed rank tests in the two-tailed configuration) were conducted. Linear regressions were conducted using Pearson's linear correlations and tested using a Student's t distribution (MATLAB *corr* function). Significance was set with alpha = 0.05 and was represented on graphs as the following: * = P < 0.05, ** = P < 0.01, ***= P < 0.001, **** = P < 0.0001. As mentioned in the figure legends, individual data-points are plotted above bars indicating mean ± SEM next to box plots (representing 25th, 50th, 75th percentile of distribution).

Figure legends

Figure 1. **Nasal pressure recordings in freely-moving mice uncovers distinct respiratory features, including pauses, across vigilance states**

A. Schematic representation of nasal cannula implantation used to monitor instantaneous respiration combined with extracellular electrophysiology in freely-moving conditions

B. Instantaneous nasal pressure (black line) monitored during two respiratory cycles of NREM sleep. They comprise inhalation (positive pressure), exhalation (negative pressure), and pauses (colored areas) periods. Dashed line: 0 p.s.i.

C. Top panels: Representative pressure traces of for respiratory signals (2 seconds) co-recorded with silicon probes implanted in the dorsal hippocampus and accelerometer across Wake, REM and NREM behavioral states. Middle panels: Spectrogram of co-recorded CA1 LFP during respiration across states. Bottom panels: Instantaneous acceleration co-recorded with neural traces. Magenta box: the two respiratory cycles shown in A.

D. Left: Respiration rate increased in Wake as compared to both REM and NREM, which was also reduced compared to REM ($F_{(2,67)}$= 500, P< 0.0001). Post-hoc comparison with Bonferroni correction showed a mean respiration rate increase during Wake as compared NREM (t_{67} = 25.8, P < 0.0001) and REM (t_{67} = 19.7, P < 0.0001), and that the rate during REM was increased when compared to NREM (t_{67} = 15.1, P < 0.0001). Top right: Inhalation duration showed a significant decrease during Wake as compared to both NREM and NREM, and REM as compared to NREM. $F_{(2,67)}$ = 535, P < 0.0001; post-hoc comparison with Bonferroni correction: between Wake and NREM: t_{67} = 27.9, P < 0.0001; between Wake and REM: t_{67} = 22.9, P< 0.0001; between NREM and REM: t_{67} = 7.5, P < 0.0001. Bottom right: duration of exhalation showed a reduction during Wake as compared to both REM and NREM and no differences between REM and NREM. $F(_{2,67)}$ = 191, P < 0.0001; post-hoc comparison with Bonferroni correction: between Wake and NREM: t_{67}= 25.1, P < 0.0001; between Wake and REM: t_{67} = 15.1, P < 0.0001; between NREM and REM: t_{67} = 1.4, P = 0.17.

E. Left: Duration of pauses after inhalation showed no significant difference between Wake and NREM, a significant increase during Wake when compared to REM and a significant increase in NREM as compared to REM. $F_{(2,67)}$ = 92.9, P< 0.0001; post-hoc comparison with Bonferroni correction: between Wake and NREM: t_{67} = 0.26, P =

0.79; between Wake and REM: t_{67} = 37.0, P < 0.0001; between NREM and REM: t_{67} = 9.6, P < 0.0001. (Right) Duration of pauses after exhalation showed a significant decrease in Wake compared to both NREM and REM and a significant increase during NREM compared to REM. $F_{(2,67)}$= 119, P < 0.0001; post-hoc comparison with Bonferroni correction: between Wake and NREM: t_{67}= 13.8, P < 0.0001; between Wake and REM: t_{67} = 14.9, P < 0.0001; between NREM and REM: t_{67} = 2.9, P = 0.005.

F. Durations of respiratory pauses after both inhalation and exhalation averaged over individual recording sessions (dots).

G. Cumulated durations of respiratory pauses (after both inhalation + exhalation) averaged over whole sessions and plotted against the mean respiration rate of the same session.

H. Left: Duration of pauses after inhalation expressed as fractions of the duration of the associated respiratory cycles. $F_{(2,67)}$ = 348, P < 0.0001; post-hoc comparison with Bonferroni correction: between Wake and NREM: t_{67} = 11.8, P < 0.0001; between Wake and REM: t_{67} = 43.7, P < 0.0001; between NREM and REM: t_{67} = 11.3, P < 0.0001. Right: Same for pauses after exhalation. Pause fractions showed a decrease in Wake compared to both NREM and REM and a smaller difference between NREM and REM. $F_{(2, 67)}$= 131, P < 0.0001; post-hoc comparison with Bonferroni correction: between wake and NREM: t_{67} = 16.3, P < 0.0001; between Wake and REM: t_{67} = 13.5, P < 0.0001; between NREM and REM: t_{67} = 2.1, P= 0.04.

Figure 2 Respiration cycle properties predict brain states

A. Supervised training strategy for the artificial neuronal network in **Supplementary Fig. 5**. Network parameters were adjusted to minimize the categorical cross-entropy between the predicted states probabilities and automated annotations of brain states based on the LFP (top) (**Methods**). For validation purpose, the training dataset included all animal recordings except for one test animal (bottom). All performance indicators were computed by grouping results from the 9 training paradigms associated to the 9 possible validation animals.

B. Prediction of brain states for a session from animal #3 which was left out of the training process (validation animal). Predicted states were chosen as the ones with highest predicted probability among the three possible states (**Methods**). Prediction confidence (blue) (the maximal predicted state probability) was also provided as an index of trust in the predicted state.

C. Median confusion matrix of prediction for all cycles, from all sessions, when each animal was alternatively used for validation. Values correspond to fractions of annotations (lines sum to 1). The median was computed over the 9 sets of results obtained with the 9 possible validation animals and each set of indicators were obtained by averaging results from 7 independently fitted networks associated to the validation animal.

D. Confusion matrices for each individual validation animal.

E. Confidence for each of the correct predictions (*Wake* as *Wake, NREM* as *NREM* and *REM* as *REM*) (n > 10e7) compared that of predictions errors (n=738661) for the validation data used in C (Kolmogorov-Smirnov test P < 10e-9).

F. Prediction performance indicators averaged over all fitted networks for each validation animals (n=9) and repetitions for each (n = 7) (total n = 63). *Recall* = (#True positive predictions)/(#annotations); *Precision* = (#True positive)/(#predictions); *F1-score* = (2 x #true positive)/(2 x #true positive + #false positive + #false negative).

G. Prediction performance after training artificial neuronal networks with missing input parameters (excluded in both training and validation). *None*: same as **F** (7 repetitions), *Volumes* + *flows*: inhalation peak flow, exhalation trough flow, inhalation and exhalation volumes, and their local standard deviations (SDs). *Inh* + *Exh kinetics*: inhalation time to peak, exhalation time to trough, inhalation and exhalation durations, and their SDs. *Pauses*: inhalation- and exhalation-associated pause durations, and their SDs. *Local SDs*: local SDs of all the 10 respiratory features. 5 repetitions were performed for each exclusion condition and each of the 9 validation animals. Statistical tests: comparison of the performance indicators for each brain state between the exclusion results and the *None* reference using the F statistics of an ANOVA with repeated measurements and two factors: validation animal index and exclusion group (*None* vs

other). The validation animal factor was always significant (P < 10e-3). Statistics for the exclusion group factor are given in **Supplementary Table 2**.

Figure 3 Distinct respiration features co-vary with brain states and animal identity

A. Correlation between features of single respiration cycles (n = 24000) after log-normalization (**Supplementary Table 1**) and the first three principal components (PCs) obtained by PCA. Proportion of brain states (Wake/NREM/REM) and animal identities (8 mice) were equalized. Inh: inhalation. Exh: exhalation.

B. Fraction of the total data variance explained by all PCs. The first three largest are denoted PC1, 2 and 3 in decreasing order of explained variance.

C. Cumulative distributions of coefficients associated to the PC1 2 and 3 (A) for the individual 8 mice (n = 3000 for each).

D. Entropy of single cycle PC coefficients computed from *Pr(animal id|coefficient value)* (**Methods**) for all PCs. Lower entropy indicates better identity predictive power.

E. Cumulative distributions of coefficients associated to Wake (n = 8000), REM (n = 8000) and NREM (n = 8000) states for all animals pooled together.

F. Entropy of single cycle PC coefficients computed from *Pr(brain state|coefficient value)* (**Methods**) for all PCs. Lower entropy indicates better identity predictive power.

Figure 4. Fast and slow adaptation of breathing at different brain state transitions

A. Time series of PC1 and 3 coefficients aligned to annotated brain states for an exemplar session. **B.** Zoom on three Wake→NREM transition events indicated in A. Arrows highlight the adaptation of the coefficients at state transitions. **C.** Zoom on three NREM→REM transition events indicated in A. **D.** Population averages of PC1 coefficients for all state transitions in the recording sessions from 65 sessions of 9 animals. Wake→NREM n = 627; NREM→Wake n = 543; NREM→REM n = 225; REM→NREM n = 164, REM→Wake n = 59. Plot: average value (solid line) ± standard value (shade). Cycles that did not match the studied states because of extra state transitions in the

analysis window were clipped out (e. g. the last NREM cycles are discarded if REM→NREM occurs after an initial NREM→REM). **E.** Same as D, but for PC3 coefficients.

References

1. Feldman JL, Del Negro CA, Gray PA. Understanding the rhythm of breathing: so near, yet so far. Annual review of physiology. 2013;75:423-52.
2. Buonviso N, Dutschmann M, Mouly AM, Wesson DW. Adaptation and Plasticity of Breathing during Behavioral and Cognitive Tasks. Neural plasticity. 2016;2016:2804205.
3. Heck DH, McAfee SS, Liu Y, Babajani-Feremi A, Rezaie R, Freeman WJ, et al. Breathing as a Fundamental Rhythm of Brain Function. Frontiers in neural circuits. 2016;10:115.
4. Wachowiak M. All in a sniff: olfaction as a model for active sensing. Neuron. 2011;71(6):962-73.
5. Kleinfeld D, Deschenes M, Wang F, Moore JD. More than a rhythm of life: breathing as a binder of orofacial sensation. Nature neuroscience. 2014;17(5):647-51.
6. Bagur S, Lacroix MM, de Lavilleon G, Lefort JM, Geoffroy H, Benchenane K. Harnessing olfactory bulb oscillations to perform fully brain-based sleep-scoring and real-time monitoring of anaesthesia depth. PLoS biology. 2018;16(11):e2005458.
7. Karalis N, Sirota A. Breathing coordinates cortico-hippocampal dynamics in mice during offline states. Nature communications. 2022;13(1):467.
8. Moore JD, Deschenes M, Furuta T, Huber D, Smear MC, Demers M, et al. Hierarchy of orofacial rhythms revealed through whisking and breathing. Nature. 2013;497(7448):205-10.
9. Tort ABL, Brankack J, Draguhn A. Respiration-Entrained Brain Rhythms Are Global but Often Overlooked. Trends in neurosciences. 2018;41(4):186-97.
10. Ito J, Roy S, Liu Y, Cao Y, Fletcher M, Lu L, et al. Whisker barrel cortex delta oscillations and gamma power in the awake mouse are linked to respiration. Nature communications. 2014;5:3572.
11. Arshamian A, Iravani B, Majid A, Lundstrom JN. Respiration Modulates Olfactory Memory Consolidation in Humans. J Neurosci. 2018;38(48):10286-94.
12. Bensafi M, Rouby C, Farget V, Bertrand B, Vigouroux M, Holley A. Perceptual, affective, and cognitive judgments of odors: pleasantness and handedness effects. Brain Cogn. 2003;51(3):270-5.
13. Brown RP, Gerbarg PL. Yoga breathing, meditation, and longevity. Annals of the New York Academy of Sciences. 2009;1172:54-62.
14. Herrero JL, Khuvis S, Yeagle E, Cerf M, Mehta AD. Breathing above the brain stem: volitional control and attentional modulation in humans. J Neurophysiol. 2018;119(1):145-59.
15. Perciavalle V, Blandini M, Fecarotta P, Buscemi A, Di Corrado D, Bertolo L, et al. The role of deep breathing on stress. Neurol Sci. 2017;38(3):451-8.

16. Zelano C, Jiang H, Zhou G, Arora N, Schuele S, Rosenow J, et al. Nasal Respiration Entrains Human Limbic Oscillations and Modulates Cognitive Function. J Neurosci. 2016;36(49):12448-67.
17. Johnson BN, Mainland JD, Sobel N. Rapid olfactory processing implicates subcortical control of an olfactomotor system. J Neurophysiol. 2003;90(2):1084-94.
18. Rozenkrantz L, Zachor D, Heller I, Plotkin A, Weissbrod A, Snitz K, et al. A Mechanistic Link between Olfaction and Autism Spectrum Disorder. Current biology : CB. 2015;25(14):1904-10.
19. Wesson DW, Donahou TN, Johnson MO, Wachowiak M. Sniffing behavior of mice during performance in odor-guided tasks. Chemical senses. 2008;33(7):581-96.
20. Adrian ED. Olfactory reactions in the brain of the hedgehog. The Journal of physiology. 1942;100(4):459-73.
21. Courtiol E, Wilson DA. Thalamic olfaction: characterizing odor processing in the mediodorsal thalamus of the rat. J Neurophysiol. 2014;111(6):1274-85.
22. Welker WI. Analysis of sniffing of the albino rat. Behaviour. 1964;22:223-44.
23. Wesson DW, Verhagen JV, Wachowiak M. Why sniff fast? The relationship between sniff frequency, odor discrimination, and receptor neuron activation in the rat. J Neurophysiol. 2009;101(2):1089-102.
24. Youngentob SL, Mozell MM, Sheehe PR, Hornung DE. A quantitative analysis of sniffing strategies in rats performing odor detection tasks. Physiology & behavior. 1987;41(1):59-69.
25. Macrides F. Temporal relationships between hippocampal slow waves and exploratory sniffing in hamsters. Behavioral biology. 1975;14(3):295-308.
26. Kepecs A, Uchida N, Mainen ZF. Rapid and precise control of sniffing during olfactory discrimination in rats. J Neurophysiol. 2007;98(1):205-13.
27. Zelano C, Bensafi M, Porter J, Mainland J, Johnson B, Bremner E, et al. Attentional modulation in human primary olfactory cortex. Nature neuroscience. 2005;8(1):114-20.
28. Bagur S, Lefort JM, Lacroix MM, de Lavilleon G, Herry C, Chouvaeff M, et al. Breathing-driven prefrontal oscillations regulate maintenance of conditioned-fear evoked freezing independently of initiation. Nature communications. 2021;12(1):2605.
29. Bloch S, Lemeignan M, Aguilera N. Specific respiratory patterns distinguish among human basic emotions. International journal of psychophysiology : official journal of the International Organization of Psychophysiology. 1991;11(2):141-54.
30. Boiten FA, Frijda NH, Wientjes CJ. Emotions and respiratory patterns: review and critical analysis. International journal of psychophysiology : official journal of the International Organization of Psychophysiology. 1994;17(2):103-28.
31. Hegoburu C, Shionoya K, Garcia S, Messaoudi B, Thevenet M, Mouly AM. The RUB Cage: Respiration-Ultrasonic Vocalizations-Behavior Acquisition Setup for Assessing Emotional Memory in Rats. Frontiers in behavioral neuroscience. 2011;5:25.
32. Yackle K, Schwarz LA, Kam K, Sorokin JM, Huguenard JR, Feldman JL, et al. Breathing control center neurons that promote arousal in mice. Science. 2017;355(6332):1411-5.
33. Matarazzo V, Caccialupi L, Schaller F, Shvarev Y, Kourdougli N, Bertoni A, et al. Necdin shapes serotonergic development and SERT activity modulating breathing in a mouse model for Prader-Willi syndrome. Elife. 2017;6.

34. Peupelmann J, Boettger MK, Ruhland C, Berger S, Ramachandraiah CT, Yeragani VK, et al. Cardio-respiratory coupling indicates suppression of vagal activity in acute schizophrenia. Schizophr Res. 2009;112(1-3):153-7.
35. Sobel N, Thomason ME, Stappen I, Tanner CM, Tetrud JW, Bower JM, et al. An impairment in sniffing contributes to the olfactory impairment in Parkinson's disease. Proc Natl Acad Sci U S A. 2001;98(7):4154-9.
36. Hardie RJ, Efthimiou J, Stern GM. Respiration and sleep in Parkinson's disease. Journal of neurology, neurosurgery, and psychiatry. 1986;49(11):1326.
37. Rice JE, Antic R, Thompson PD. Disordered respiration as a levodopa-induced dyskinesia in Parkinson's disease. Mov Disord. 2002;17(3):524-7.
38. Ming X, Patel R, Kang V, Chokroverty S, Julu PO. Respiratory and autonomic dysfunction in children with autism spectrum disorders. Brain Dev. 2016;38(2):225-32.
39. Luppi PH, Chancel A, Malcey J, Cabrera S, Fort P, Maciel RM. Which structure generates paradoxical (REM) sleep: The brainstem, the hypothalamus, the amygdala or the cortex? Sleep Med Rev. 2024;74:101907.
40. Saper CB, Fuller PM, Pedersen NP, Lu J, Scammell TE. Sleep state switching. Neuron. 2010;68(6):1023-42.
41. Siegel JM. The neurobiology of sleep. Semin Neurol. 2009;29(4):277-96.
42. Adamantidis AR, Gutierrez Herrera C, Gent TC. Oscillating circuitries in the sleeping brain. Nature reviews Neuroscience. 2019;20(12):746-62.
43. Girin B, Juventin M, Garcia S, Lefevre L, Amat C, Fourcaud-Trocme N, et al. The deep and slow breathing characterizing rest favors brain respiratory-drive. Scientific reports. 2021;11(1):7044.
44. Schreck MR, Zhuang L, Janke E, Moberly AH, Bhattarai JP, Gottfried JA, et al. State-dependent olfactory processing in freely behaving mice. Cell reports. 2022;38(9):110450.
45. Oudiette D, Dodet P, Ledard N, Artru E, Rachidi I, Similowski T, et al. REM sleep respiratory behaviours mental content in narcoleptic lucid dreamers. Scientific reports. 2018;8(1):2636.
46. Remmers JE. Sleeping and breathing. Chest. 1990;97(3 Suppl):77S-80S.
47. Hammer M, Jung F, Brankack J, Yanovsky Y, Tort ABL, Draguhn A. Respiration and rapid eye movement (REM) sleep substructure: short versus long episodes. Journal of sleep research. 2023;32(3):e13777.
48. Noto T, Zhou G, Schuele S, Templer J, Zelano C. Automated analysis of breathing waveforms using BreathMetrics: a respiratory signal processing toolbox. Chemical senses. 2018;43(8):583-97.
49. Yamauchi M, Ocak H, Dostal J, Jacono FJ, Loparo KA, Strohl KP. Post-sigh breathing behavior and spontaneous pauses in the C57BL/6J (B6) mouse. Respir Physiol Neurobiol. 2008;162(2):117-25.
50. Shusterman R, Smear MC, Koulakov AA, Rinberg D. Precise olfactory responses tile the sniff cycle. Nature neuroscience. 2011;14(8):1039-44.
51. Smear M, Shusterman R, O'Connor R, Bozza T, Rinberg D. Perception of sniff phase in mouse olfaction. Nature. 2011;479(7373):397-400.

52. Verhagen JV, Wesson DW, Netoff TI, White JA, Wachowiak M. Sniffing controls an adaptive filter of sensory input to the olfactory bulb. Nature neuroscience. 2007;10(5):631-9.
53. Wilson CD, Serrano GO, Koulakov AA, Rinberg D. A primacy code for odor identity. Nature communications. 2017;8(1):1477.
54. Rayan A, Agarwal A, Samanta A, Severijnen E, van der Meij J, Genzel L. Sleep scoring in rodents: Criteria, automatic approaches and outstanding issues. The European journal of neuroscience. 2024;59(4):526-53.
55. Mizuseki K, Sirota A, Pastalkova E, Buzsaki G. Theta oscillations provide temporal windows for local circuit computation in the entorhinal-hippocampal loop. Neuron. 2009;64(2):267-80.
56. Grosmark AD, Mizuseki K, Pastalkova E, Diba K, Buzsaki G. REM sleep reorganizes hippocampal excitability. Neuron. 2012;75(6):1001-7.
57. Jessberger J, Zhong W, Brankack J, Draguhn A. Olfactory Bulb Field Potentials and Respiration in Sleep-Wake States of Mice. Neural plasticity. 2016;2016:4570831.
58. Levenstein D, Buzsaki G, Rinzel J. NREM sleep in the rodent neocortex and hippocampus reflects excitable dynamics. Nature communications. 2019;10(1):2478.
59. Bolding KA, Franks KM. Complementary codes for odor identity and intensity in olfactory cortex. Elife. 2017;6.
60. Grimaud J, Murthy VN. How to monitor breathing in laboratory rodents: a review of the current methods. J Neurophysiol. 2018;120(2):624-32.
61. Liu S, Han S. Simultaneous recording of breathing and neural activity in awake behaving mice. STAR Protoc. 2022;3(2):101412.
62. McAfee SS, Ogg MC, Ross JM, Liu Y, Fletcher ML, Heck DH. Minimally invasive highly precise monitoring of respiratory rhythm in the mouse using an epithelial temperature probe. Journal of neuroscience methods. 2016;263:89-94.
63. Reisert J, Golden GJ, Matsumura K, Smear M, Rinberg D, Gelperin A. Comparing thoracic and intra-nasal pressure transients to monitor active odor sampling during odor-guided decision making in the mouse. Journal of neuroscience methods. 2014;221:8-14.
64. Mutlu K, Rabell JE, Martin Del Olmo P, Haesler S. IR thermography-based monitoring of respiration phase without image segmentation. Journal of neuroscience methods. 2018;301:1-8.
65. Esquivelzeta Rabell J, Mutlu K, Noutel J, Martin Del Olmo P, Haesler S. Spontaneous Rapid Odor Source Localization Behavior Requires Interhemispheric Communication. Current biology : CB. 2017;27(10):1542-8 e4.
66. Uchida N, Mainen ZF. Speed and accuracy of olfactory discrimination in the rat. Nature neuroscience. 2003;6(11):1224-9.
67. Wesson DW. Sniffing behavior communicates social hierarchy. Current biology : CB. 2013;23(7):575-80.
68. Liu Y, McAfee SS, Heck DH. Hippocampal sharp-wave ripples in awake mice are entrained by respiration. Scientific reports. 2017;7(1):8950.
69. Liao SM, Kleinfeld D. A change in behavioral state switches the pattern of motor output that underlies rhythmic head and orofacial movements. Current biology : CB. 2023;33(10):1951-66 e6.

70. Courtiol E, Lefevre L, Garcia S, Thevenet M, Messaoudi B, Buonviso N. Sniff adjustment in an odor discrimination task in the rat: analytical or synthetic strategy? Frontiers in behavioral neuroscience. 2014;8:145.
71. Merle L, Person O, Bonnet P, Gregoire S, Soubeyre V, Grosmaitre X, et al. Maternal high fat high sugar diet disrupts olfactory behavior but not mucosa sensitivity in the offspring. Psychoneuroendocrinology. 2019;104:249-58.
72. Fontanini A, Spano P, Bower JM. Ketamine-xylazine-induced slow (< 1.5 Hz) oscillations in the rat piriform (olfactory) cortex are functionally correlated with respiration. J Neurosci. 2003;23(22):7993-8001.
73. Macrides F, Chorover SL. Olfactory bulb units: activity correlated with inhalation cycles and odor quality. Science. 1972;175(4017):84-7.
74. Courtiol E, Hegoburu C, Litaudon P, Garcia S, Fourcaud-Trocme N, Buonviso N. Individual and synergistic effects of sniffing frequency and flow rate on olfactory bulb activity. J Neurophysiol. 2011;106(6):2813-24.
75. Fukunaga I, Berning M, Kollo M, Schmaltz A, Schaefer AT. Two distinct channels of olfactory bulb output. Neuron. 2012;75(2):320-9.
76. Yanovsky Y, Ciatipis M, Draguhn A, Tort AB, Brankack J. Slow oscillations in the mouse hippocampus entrained by nasal respiration. J Neurosci. 2014;34(17):5949-64.
77. Nguyen Chi V, Muller C, Wolfenstetter T, Yanovsky Y, Draguhn A, Tort AB, et al. Hippocampal Respiration-Driven Rhythm Distinct from Theta Oscillations in Awake Mice. J Neurosci. 2016;36(1):162-77.
78. Bastianini S, Alvente S, Berteotti C, Lo Martire V, Silvani A, Swoap SJ, et al. Accurate discrimination of the wake-sleep states of mice using non-invasive whole-body plethysmography. Scientific reports. 2017;7:41698.
79. Geuther B, Chen M, Galante RJ, Han O, Lian J, George J, et al. High-throughput visual assessment of sleep stages in mice using machine learning. Sleep. 2022;45(2).
80. Del Negro CA, Funk GD, Feldman JL. Breathing matters. Nature reviews Neuroscience. 2018;19(6):351-67.
81. Richter DW, Smith JC. Respiratory rhythm generation in vivo. Physiology (Bethesda). 2014;29(1):58-71.
82. Anderson TM, Ramirez JM. Respiratory rhythm generation: triple oscillator hypothesis. F1000Research. 2017;6:139.
83. Anderson TM, Garcia AJ, 3rd, Baertsch NA, Pollak J, Bloom JC, Wei AD, et al. A novel excitatory network for the control of breathing. Nature. 2016;536(7614):76-80.
84. De Backer WA. Central sleep apnoea, pathogenesis and treatment: an overview and perspective. Eur Respir J. 1995;8(8):1372-83.
85. Bartolucci ML, Berteotti C, Alvente S, Bastianini S, Guidi S, Lo Martire V, et al. Obstructive sleep apneas naturally occur in mice during REM sleep and are highly prevalent in a mouse model of Down syndrome. Neurobiology of disease. 2021;159:105508.
86. Bastianini S, Alvente S, Berteotti C, Bosi M, Lo Martire V, Silvani A, et al. Post-sigh sleep apneas in mice: Systematic review and data-driven definition. Journal of sleep research. 2019;28(6):e12845.

87. Heinzer R, Vat S, Marques-Vidal P, Marti-Soler H, Andries D, Tobback N, et al. Prevalence of sleep-disordered breathing in the general population: the HypnoLaus study. Lancet Respir Med. 2015;3(4):310-8.
88. Maiolino G, Bisogni V, Silvani A, Pengo MF, Lombardi C, Parati G. Treating sleep disorders to improve blood pressure control and cardiovascular prevention: a dream come true?-a narrative review. J Thorac Dis. 2020;12(Suppl 2):S225-S34.
89. Bradley TD, Floras JS. Sleep apnea and heart failure: Part II: central sleep apnea. Circulation. 2003;107(13):1822-6.
90. Robinson TE, Kramis RC, Vanderwolf CH. Two types of cerebral activation during active sleep: relations to behavior. Brain Res. 1977;124(3):544-9.
91. Sirota A, Montgomery S, Fujisawa S, Isomura Y, Zugaro M, Buzsaki G. Entrainment of neocortical neurons and gamma oscillations by the hippocampal theta rhythm. Neuron. 2008;60(4):683-97.
92. Soria-Gomez E, Bellocchio L, Reguero L, Lepousez G, Martin C, Bendahmane M, et al. The endocannabinoid system controls food intake via olfactory processes. Nature neuroscience. 2014;17(3):407-15.

Acknowledgments

We warmly thank Dmitry Rinberg and Christopher Wilson for sharing methodological details regarding nasal cannula implants. We thank the Zelano lab past and current members of the Buzsáki Lab, for making the Breathmetrics Toolbox and other scripts available. This work was supported by CNRS (L.R., F.G.), INSERM (N.C.), the Ministère de l'Enseignement Supérieur et de la Recherche (to C.M.), European Research Council (ERC-StG- 851560 to L.R.), Bordeaux University (2017 IdEx Junior Chair to L.R.), Fondation pour la Recherche Médicale and Fondation Schlumberger pour l'Education et la Recherche (FSER202112014572 to L.R.). We thank the Animal Facility of the Broca Institute (Pôle In Vivo) for mouse care and the Roux lab members for useful discussions.

Figures

Figure 1

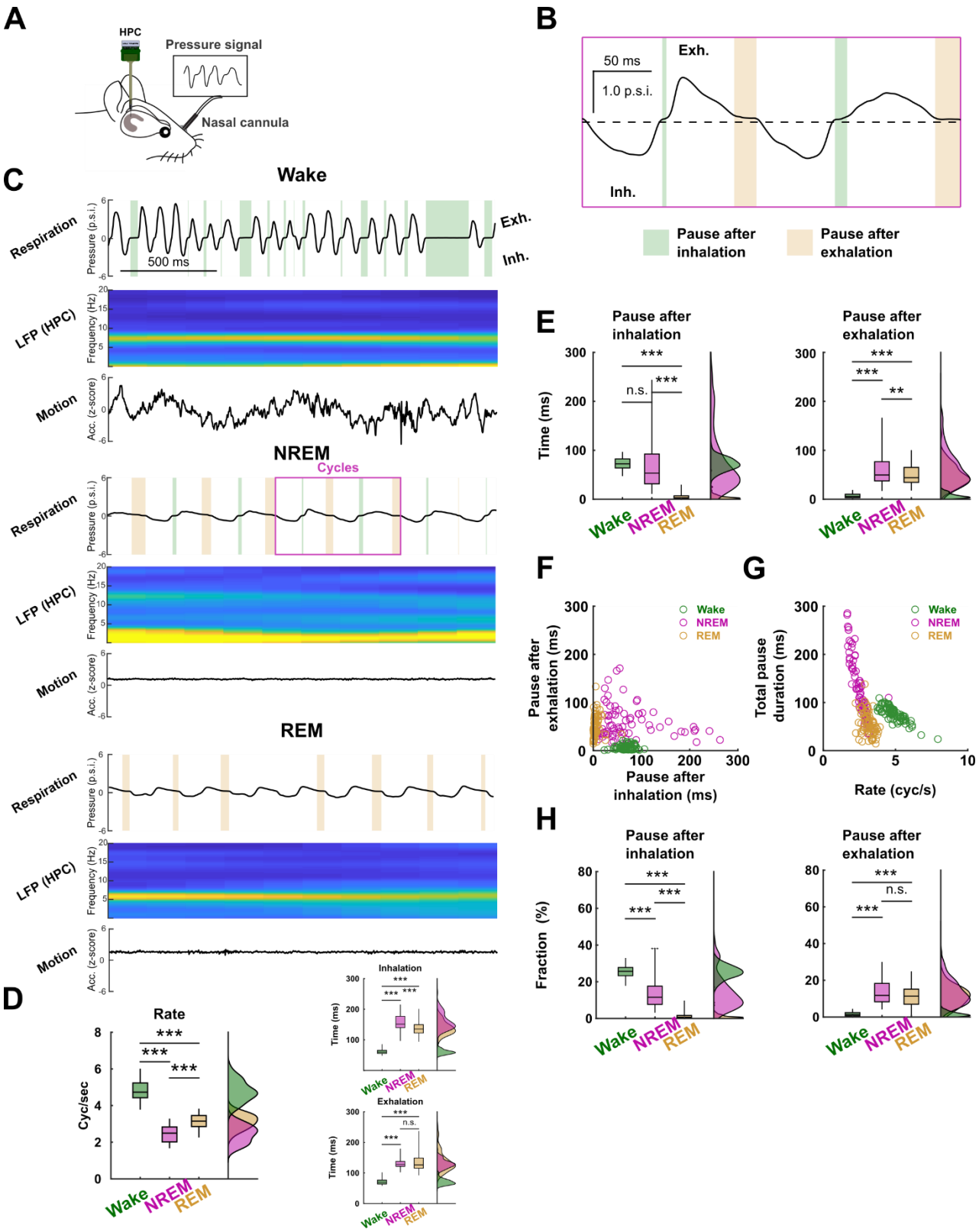
A
HPC
Pressure signal
Nasal cannula
B
50 ms
1.0 p.s.i.
Exh.
Inh.
Pause after inhalation
Pause after exhalation
C
Wake
Respiration
Pressure (p.s.i.)
500 ms
Exh.
Inh.
LFP (HPC)
Frequency (Hz)
Motion
Acc. (z-score)
NREM
Cycles
REM
D
Rate
Cyc/sec
Wake
NREM
REM
Inhalation
Exhalation
Time (ms)
n.s.
E
Pause after inhalation
Pause after exhalation
Time (ms)
F
Pause after exhalation (ms)
Pause after inhalation (ms)
G
Total pause duration (ms)
Rate (cyc/s)
H
Fraction (%)

Figure 2

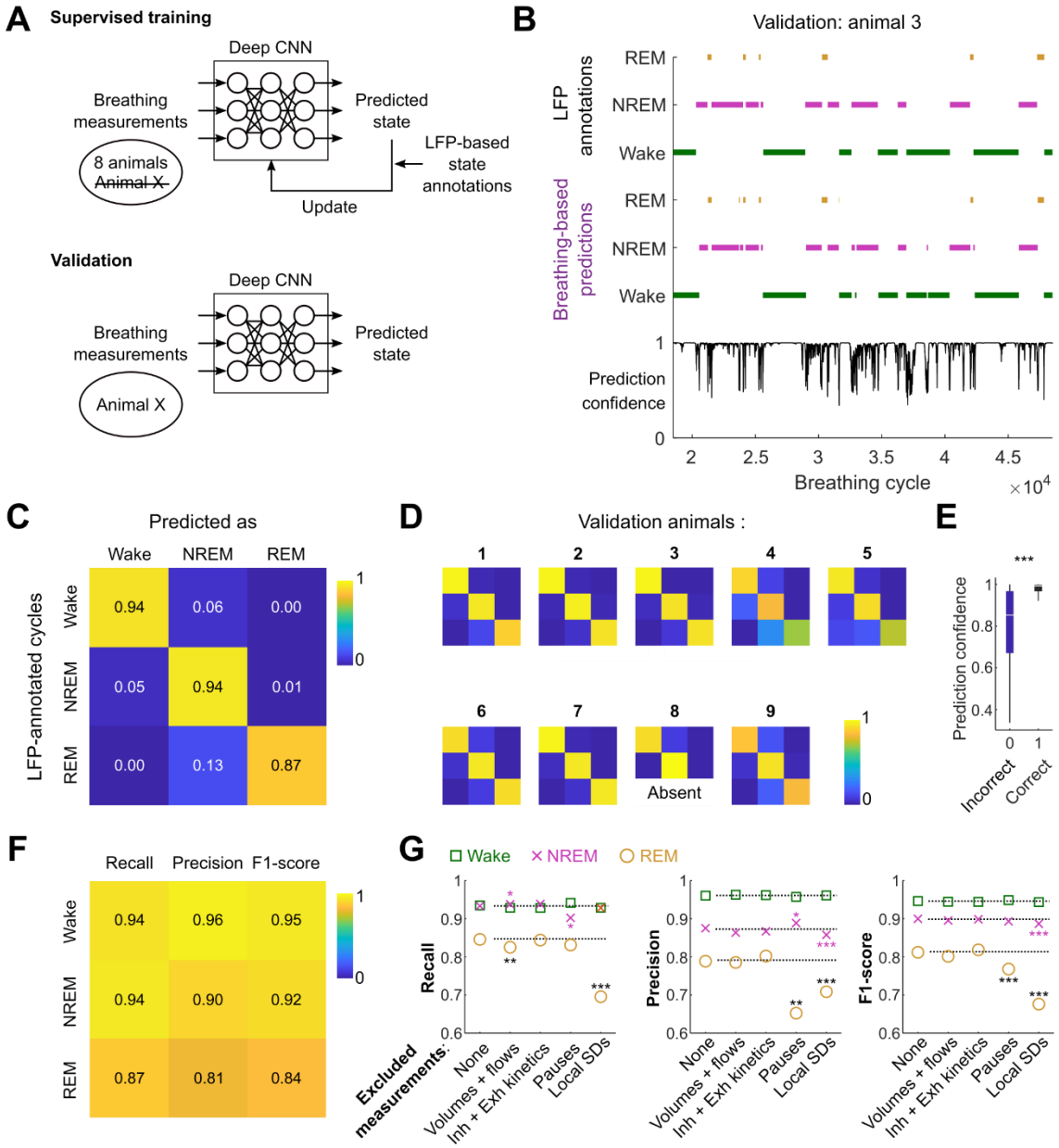
A
Supervised training
Deep CNN
Breathing measurements
8 animals
Animal X
Predicted state
LFP-based state annotations
Update
Validation
Deep CNN
Breathing measurements
Animal X
Predicted state
B
Validation: animal 3
LFP annotations
REM
NREM
Wake
Breathing-based predictions
REM
NREM
Wake
Prediction confidence
1
0
2
2.5
3
3.5
4
4.5
Breathing cycle
×10^4
C
Predicted as
Wake
NREM
REM
LFP-annotated cycles
Wake
NREM
REM
0.94
0.06
0.00
0.05
0.94
0.01
0.00
0.13
0.87
1
0
D
Validation animals :
1
2
3
4
5
6
7
8
9
Absent
1
0
E
Prediction confidence
1
0.8
0.6
0.4
0
1
Incorrect
Correct
***
F
Recall
Precision
F1-score
Wake
NREM
REM
0.94
0.96
0.95
0.94
0.90
0.92
0.87
0.81
0.84
1
0
G
Wake
NREM
REM
Recall
Precision
F1-score
1
0.9
0.8
0.7
0.6
Excluded measurements:
None
Volumes + flows
Inh + Exh kinetics
Pauses
Local SDs

Figure 3

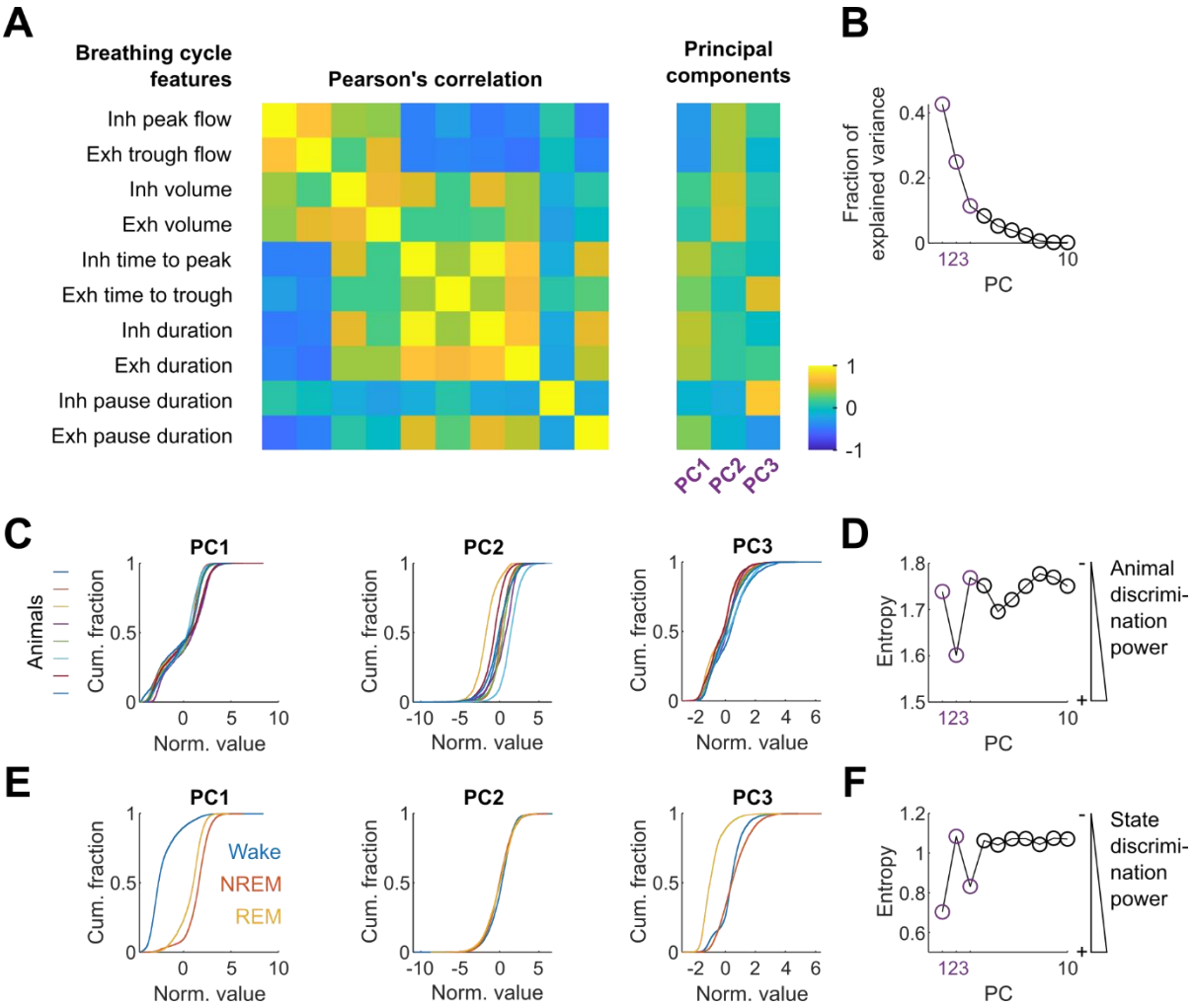
A
Breathing cycle features
Pearson's correlation
Principal components
Inh peak flow
Exh trough flow
Inh volume
Exh volume
Inh time to peak
Exh time to trough
Inh duration
Exh duration
Inh pause duration
Exh pause duration
PC1
PC2
PC3
B
Fraction of explained variance
PC
C
Animals
Cum. fraction
Norm. value
D
Entropy
Animal discrimi-nation power
E
Wake
NREM
REM
F
State discrimi-nation power

Figure 4

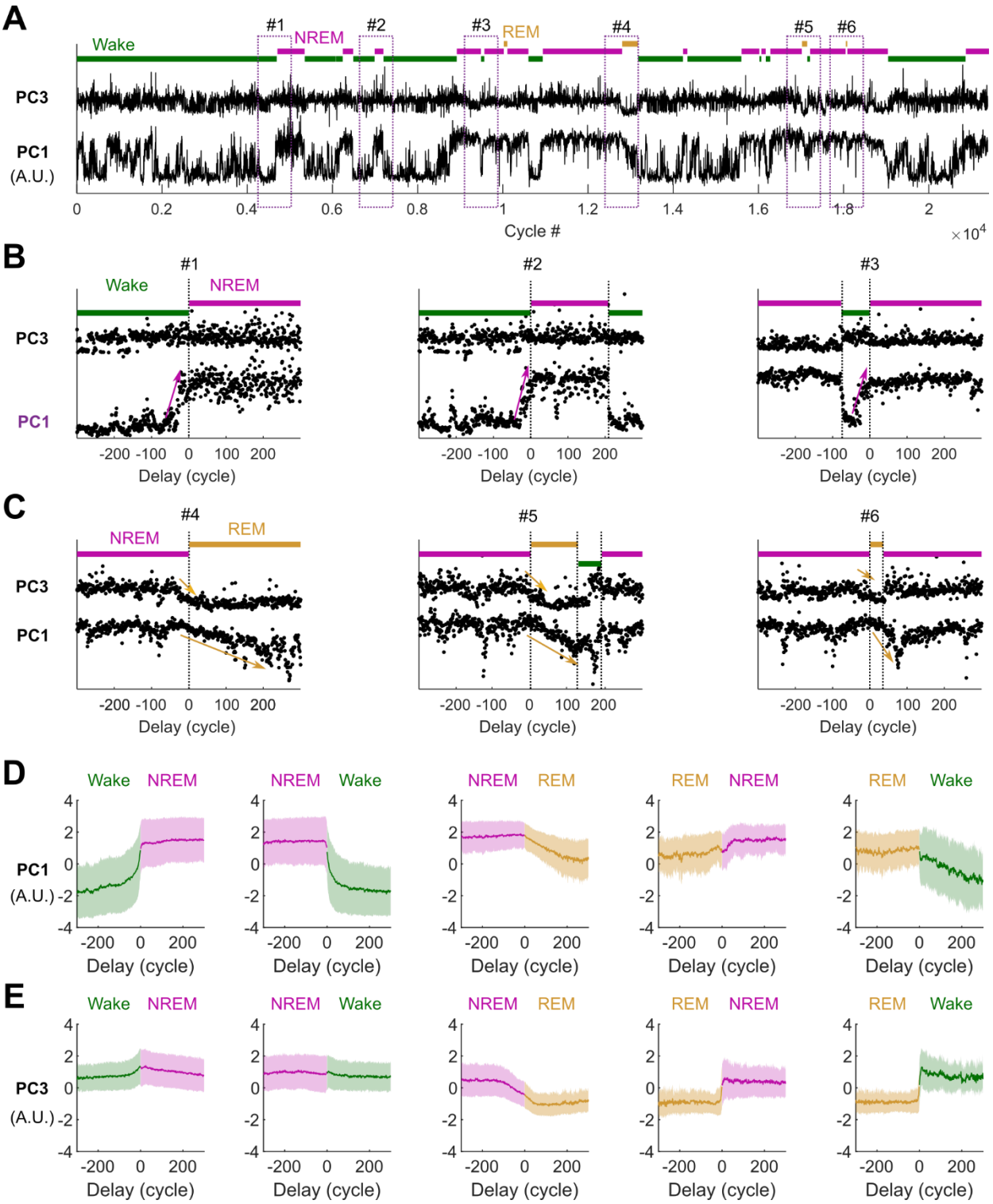
A
Wake
NREM
REM
#1
#2
#3
#4
#5
#6
PC3
PC1
(A.U.)
Cycle #
×10^4
B
Wake
NREM
PC3
PC1
Delay (cycle)
C
NREM
REM
PC3
PC1
Delay (cycle)
D
Wake NREM
NREM Wake
NREM REM
REM NREM
REM Wake
PC1
(A.U.)
Delay (cycle)
E
Wake NREM
NREM Wake
NREM REM
REM NREM
REM Wake
PC3
(A.U.)
Delay (cycle)